CFA/VISHNO 2016

Etude d'écoulement dans un canal avec des formes différentes : simulation, modélisation et validation

A. Van Hirtum
CNRS/Grenoble Univ., 11 rue de Mathématique, 38000 Grenoble, France
annemie.vanhirtum@grenoble-inp.fr

Des modéles simplifiés d'interaction fluide-structure-acoustique sont utilisés pour décrire des phénomènes complexes comme la production de la parole humaine. Ces modelés se base sur une approximation bidimensionnelle de l'écoulement dans la glotte ou dans le conduit vocal. Cette approximation est raisonnable dans le cas d'un canal avec une section transversal de forme rectangulaire. Des observations de la géométrie de la glotte et de conduit vocal lors de la production de la parole mets en évidence des formes de section très variable et donc on peut mettre en question l'assomption bidimensionnelle. Ce papier compare des données d'écoulement issue de simulation numérique tridimensionnelle, modélisation et expérience afin de montrer l'effet de la forme de la section transversal sur l'écoulement. En particulier, un canal uniforme est étudie dans laquelle une constriction est inséré. Trois constrictions sont considèré : circulaire, elliptique et secteur circulaire.

1 Introduction

Human speech sound production is a striking example of a pressure-driven phenomenon. In general, speech production models rely on simplifications based on a non-dimensional analysis of the governing Navier-Stokes equations [2]. Accounting for typical values of physiological, geometrical and flow characteristics result in non-dimensional numbers which allows one to assume the flow as incompressible [Mach number, $Ma^2 \ll 0.1$], laminar [Reynolds number $Re \approx O(10^3)$], quasi-steady [Strouhal number $Sr \ll 1$] and quasi-one-dimensional (quasi-1D) or two-dimensional (2D) based on the channel's mean aspect ratio ($Ar \geq 4$) corresponding to the width-to-height ratio of the cross-section. Therefore, quasi-1D or 2D flow models derived from boundary layer theory [2] have proven to be extremely useful to capture the underlying physics and are applied to mimic and predict ongoing phenomena using few computational resources while allowing experimental validation on replicas with a different degree of complexity. Nevertheless, the assumption of a 1D or 2D geometry implies that details of the cross-section shape perpendicular to the streamwise flow direction (x) are neglected. Viscous effects, which will dominate boundary layer development and hence flow development at low Reynolds numbers, depend on the cross-section shape [5, 2]. A quasi-three dimensional (quasi-3D) flow model was proposed [5, 4] as an extension of the quasi-1D and 2D flow models. The relevance of a quasi-3D flow model on the on onset pressure of the fluid-structure instability driven voiced speech production was shown since it increased (ellipse) or decreased (circular sector) [3]. Nevertheless, a validation of the proposed quasi-3D model is lacking. Therefore, in the current work the quasi-3D model is validated against experimental and numerical data.

2 Flow model

For a given fluid under the assumption of pressure-driven, steady, laminar and incompressible flow, the streamwise momentum equation of the governing Navier-Stokes equation is approximated using volume flow rate conservation $d\Phi/dx = 0$, as [5, 4] :

$$-\frac{\Phi^2}{A^3}\frac{dA}{dx} + \frac{1}{\rho}\frac{dP}{dx} = \nu\left(\frac{\partial^2 u}{\partial y^2} + \frac{\partial^2 u}{\partial z^2}\right), \qquad (1)$$

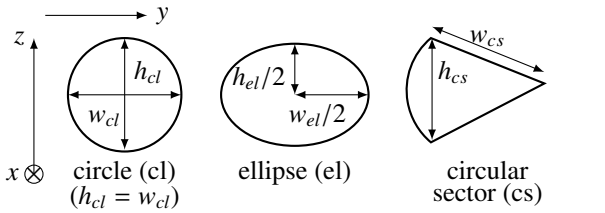

FIGURE 1 – Schematic front view ((y, z) plane) and area A for circle (cl), ellipse (el) and circular sector (cs). Spanwise extent w (y-direction) and transverse extent h (z-direction) are indicated.

with streamwise direction x, spanwise direction y, transverse direction z, driving pressure gradient dP/dx, cross-sectional area $A(x)$, local velocity $u(x, y, z)$, volume flow rate Φ, fluid density ρ (1.2kg/m^3 for air) and kinematic viscosity ν (1.5×10^{-5}m^2/s for air). The flow model accounts for viscosity (right hand term) as well as flow inertia (first source term at the left hand side) and depends therefore on the area as well as on the shape of the cross-section. It is seen that for a uniform channel, so that $dA/dx = 0$ holds, 1 reduces to purely viscous flow [5, 2]. The same way, it is seen that 1 reduces to Euler's equation describing Bernoulli flow when viscosity is neglected, *i.e.* $\nu = 0$ as for an ideal inviscid flow [2].

The flow model allows to describe flow through a uniform circular flow channel of area A_0 containing a constriction of constant length L_c and with minimum area A_c as illustrated in Fig. 2. In general, the constricted channel contains a convergent-divergent portion so that the flow separates from the walls along the divergent portion at position x_s associated with channel area A_s resulting in jet formation downstream from the constricted portion. The position of flow separation in the model is determined following an *ad-hoc* criterion $A_s = c_s \times A_c$ with $c_s = 1.2$ in accordance with literature [4]. The pressure downstream from the flow separation point P_d and other flow model outcome are assumed to be constant, *i.e.* $P_d = 0$ holds for $x \geq x_s$ (Fig. 2) which corresponds to the assumption of a stable non-expanding straight jet with infinite potential core extent x_{pc}^{∞} implying non-viscous flow as depicted in Fig. 2. Imposing upstream pressure P_0 allows then to impose the total driving pressure difference $\Delta P = P_0 - P_d$.

The pressure distribution $P(x,t)$ for $x_0 \leq x \leq x_s$ is then expressed as a quadratic equation of volume flow rate Φ [5, 4] :

$$\begin{aligned} P(x,t) = \quad & P_0 - \tfrac{1}{2}\rho\Phi^2\left(\tfrac{1}{A^2(x,t)} - \tfrac{1}{A^2(x_0)}\right) \\ & +\mu\Phi\int_{x_0}^{x}\tfrac{dx}{\beta(x,t)}, if\, x_0 \leq x < x_s, \\ P(x,t) = \quad & P_d, \qquad if\, x \geq x_s, \end{aligned} \tag{2}$$

with upstream pressure P_0, downstream pressure P_d, dynamic viscosity $\mu = \rho \cdot \nu$ (1.8×10^{-5}Pa·s for air), β is introduced to express the viscous contribution to the pressure drop and depends on the cross-section shape. For each cross-section shape, β is obtained from the analytical solution – using separation of variables and applying the no-slip boundary condition of zero velocity at the channel walls– of a classical Dirichlet problem representing the reduced streamwise momentum equation describing viscous flow through a uniform channel [5, 4]. Expressions of β for the shapes shown in Fig. 1 are given in Table 1 [5]. In addition, volume flow rate Φ is estimated as :

$$\begin{aligned} \Phi = \quad & \left[\mu\int_{x_0}^{x_s}\tfrac{dx}{\beta(x,t)} + \left\{\left(\mu\int_{x_0}^{x_s}\tfrac{dx}{\beta(x,t)}\right)^2\right.\right. \\ & \left.\left. + \; 2(P_0 - P_d)\rho\left(1/A_s^2 - 1/A^2(x_0)\right)\right\}^{1/2}\right] \\ & \times\left[\rho\left(1/A_s^2 - 1/A^2(x_0)\right)\right]^{-1}. \end{aligned} \tag{4}$$

Once volume flow rate Φ is known, the velocity profile along each cross-section can be estimated as [5] :

$$u(y,z) = \Phi\frac{\alpha(w,h,y,z)}{\beta(w,A)}, \tag{5}$$

with $\beta(w,A)$ defined in Table 1 and $\alpha(w,h,y,z)$ in Table 2. Note that geometrical parameters (w,h,A) depend on the streamwise position x.

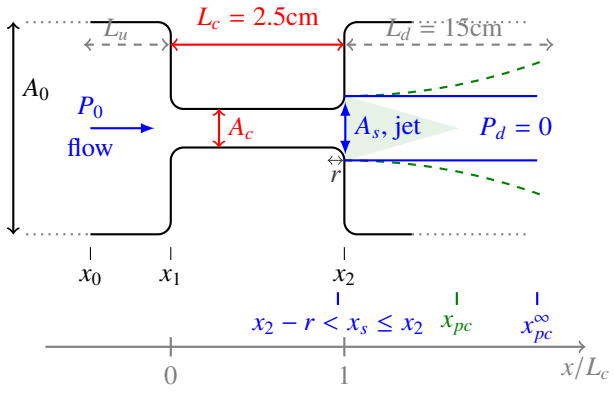

FIGURE 2 – Illustration of pressure driven flow through a uniform circular channel (area $A_0 = 490\text{mm}^2$) enveloping a constricted portion (area $A_c = 79\text{mm}^2$ and length $L_c = 2.5$cm and $r = 0.5$mm) for which the cross-section shape can be varied (Fig. 1). A non-expanding stable straight jet (full line) with infinite potential core extent x_{pc}^{∞} and a developing jet (dashed curved line) with finite potential core extent x_{pc} (shaded area) are depicted.

TABLEAU 1 – β as a function of length w and area A for cross-section shapes depicted in Fig. 1 [5]. For simplicity subscripts (cl, el and cs) are omitted.

Shape	$\beta(w,A)$
circle	$\dfrac{A^2}{\pi 8}$
ellipse	$\dfrac{w^2A^3}{(\pi^2w^4 + 16A^2)}$
circular sector$^{(a)}$	$\dfrac{w^4}{4}\left[\dfrac{\tan 2A/w^2 - 2A/w^2}{4} - \dfrac{512A^4}{\pi^5w^8}\right.$ $\left.\sum_{n=1,3...}^{\infty}\dfrac{1}{n^2(n+4A/\pi w^2)^2(n-4A/\pi w^2)}\right]$

TABLEAU 2 – α as a function of spanwise length w and transverse length h for cross-section shapes depicted in Fig. 1 [5]. Subscripts (cl, el and cs) are omitted.

Shape	$\alpha(w,h,y,z)$
circle	$\dfrac{w^2}{4} - \dfrac{(y^2+z^2)}{4}$
ellipse	$\dfrac{1}{2}\dfrac{w^2h^2}{w^2+h^2}\left(1 - \dfrac{y^2}{w^2} - \dfrac{z^2}{h^2}\right)$
circular sector$^{(a,b,c)}$	$-\dfrac{1}{4}\left[r^2\left(1 - \dfrac{\cos 2\theta}{\cos\varphi}\right) - \dfrac{16w^2\varphi^2}{\pi^3}\times\right.$ $\sum_{n=1,3...}^{\infty}(-1)^{\frac{n+1}{2}}\left(\dfrac{r}{w}\right)^{\frac{n\pi}{\varphi}}$ ... $\left.\ldots\dfrac{\cos(n\pi\theta/\varphi)}{n(n+2\varphi/\pi)(n-2\varphi/\pi)}\right]$

In the following, an abrupt constriction for which sharp edges are rounded (radius r in Fig. 2) is considered so that $A(x_2) < 1.22 \times A_c$. In this case, flow separation will occur along the rounded trailing edge of the constriction in the range $x_2 - r < x_s \leq x_2$ with $A_c < A_s \leq A(x_2) < 1.22 \times A_c$. The lower bound $x_2 - r < x_s$ implies that the pressure within the constriction is expected to become negative since $A_c < A_s$ [4] which would not be the case when a sharp non-rounded trailing edge was considered for which $A_s = A_c$. Moreover, the position of flow separation x_s along a convergent wall portion is known to shift downstream as volume flow rate Φ, or equivalently Reynolds number Re, decreases [4]. Consequently, the upper bound $x_s \leq x_2$ limits the possible downstream shift of x_s and therefore also the potential impact of volume flow rate on the flow separation position since $A_s < 1.22 \times A_c$ holds regardless the imposed volume flow rate. In addition, rounding outlet edges with such a small radius will avoid occurrence of the so-called Coanda effect which is not the case when a more convergent constriction outlet is used [2]. The same way, rounding leading edges at the inlet of the constriction aims to reduce a potential vena contracta effect in comparison with sharp inlet edges. Consequently, rounded edges

allow to focus on the impact of the cross-section area by reducing other effects related to the constriction geometry. Finally, it is noted that with respect to physiological flow applications round edges are more pertinent.

In addition, an adaptive immersed boundary (IB) method is used for the simulations [1] pressure-driven incompressible laminar air flow through a constricted channel as depicted in Fig. 2. IB uses a Lagrangian description of the immersed structure, along with an Eulerian description of the momentum, velocity, and incompressibility of the coupled fluid-structure system.

In order to study the effect of cross-sectional shape (circle, ellipse, elliptical sector in Fig. 1), all other geometrical parameters are constant (L_c = 2.5cm and A_c = 79mm^2). Concrete values of geometrical characteristics (spanwise length $w_.$, transverse length $h_.$) indicated in Fig. 1 for the circle, ellipse and circular sector (with opening angle of 30°) are summarized in Table 3. In addition, the associated hydraulic diameter $D = 4A/P$, proportional to the ratio of cross-sectional area A and its wetted perimeter P [5], is given. From the

Tableau 3 – Overview of geometrical constriction parameters (see Fig. 1).

	circle	ellipse	circular sector
D [mm]	10	6.7	7.2
w [mm]	10	22.4	17.3
h [mm]	10	4.5	9.0

A_c = 79mm^2, L_c = 25mm

magnitude of the hydraulic diameter D and assuming similar Φ and A_c, the bulk Reynolds number $Re = \frac{\Phi D}{\nu A_c}$ associated with the different cross-sections can be listed in descending order as circle, ellipse and circular sector. Therefore, following a reasoning based on decreasing Reynolds number, viscous effects are likely to be most notable for the circular sector [2].

3 Experiments

In comparison with the numerical grid, the constriction's streamwise extrema are prolonged in order to add screwthread (Fig. 3) so that an upstream and downstream circular tube with area A_0 = 490mm^2 (or diameter D_0 = 25mm so that $L_c = 1 \times D_0$) can be attached air-tightly. Consequently, the constriction degree of the flow channel yields again 84%. The downstream tube has length L_d = 15cm ($\approx 7 \times D_0$) as was the case for numerical simulations. The upstream tube on the other hand has length L_u = 5cm ($\approx 2 \times D_0$) in the numerical grid whereas the length of the downstream tube used in

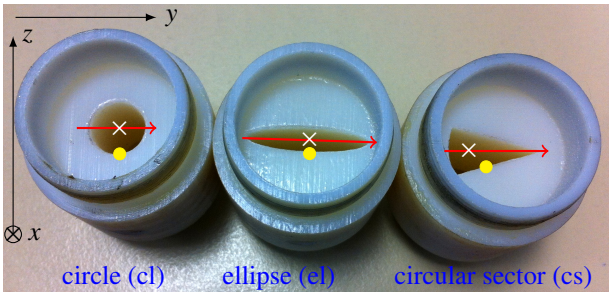

Figure 3 – Illustration of cross-sectional shapes ((y, z) plane) as depicted in Fig. 1. Position of pressure tap P_1 (•) and direction of velocity profiles along the major axis (⟶, spanwise profiles) are depicted. The cross-sectional position (×) of longitudinal velocity profiles is indicated as well.

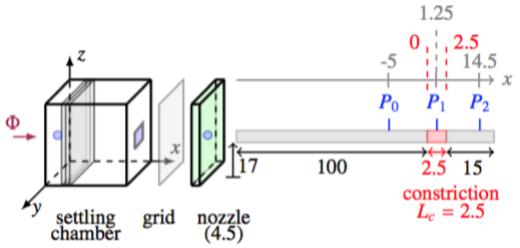

Figure 4 – Setup for pressure measurements [cm].

the experiments yields L_u = 1m ($\approx 50 \times D_0$) in order to favor laminar flow at the inlet of the constriction during the experiments [2].

Pressure sensors (Kulite XCS-093) can be positioned in pressure taps $P_{0,1,2}$ as illustrated in Fig. 4 [4]. The flow velocity downstream from the constriction is measured by hot film anemometry [4]. Spanwise velocity profiles are gathered by positioning the hot film at a distance < 1mm downstream from the center of the nozzle exit and displacing the hot film with a spanwise step of 0.5mm parallel to the cross-section exit plane across the direction depicted in Fig. 3. Longitudinal velocity profiles in the near field downstream from the constriction for elliptical and circular sector cross-section shape are obtained by positioning the hot film at a distance < 1mm downstream from the nozzle exit at the cross-sectional position associated with the centerline of the jet, *i.e.* $(w_{cl}/2, h_{cl}/2)$ for circle, $(w_{el}/2, h_{el}/2)$ for ellipse and $(w_{cs} \times 0.3, h_{cs}/2)$ for circular sector as illustrated in Fig. 3 [5, 4].

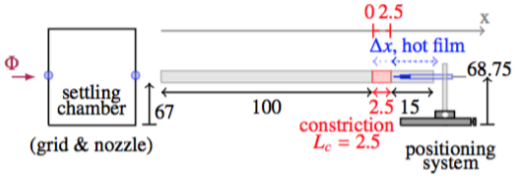

Figure 5 – Setup to measure the velocity field [cm].

4 Quasi-3D model validation

4.1 Qualitative model evaluation

4.1.1 Pressure within the constriction

From 2 is seen that the pressure drop purely due to flow inertia, *i.e.* without viscosity, expressed as ratio P_x/P_0 between the pressure somewhere within the uniform portion of the constriction ($P_x = P(x)$ with $x_1 < x < x_2$ in Fig. 2) and upstream from the constriction (P_0 at $x = x_0$) depends solely on the geometry as $P_x/P_0 \approx 1-(A_s/A_c)^2$ with $A_s \approx 95\text{mm}^2$ and $A_c = 79\text{mm}^2$ and neglecting $A_0 = 490\text{mm}^2$. Therefore, the ratio P_x/P_0 is constant within the constricted portion and yields about 145% independently from cross-section shape or applied volume flow rate Φ. From 2 is seen that viscosity is expected to reduce this pressure drop. In contrast to the term expressing flow inertia, the viscous term depends on volume flow rate Φ, and hence bulk Reynolds number Re, as well as on the cross-section shape as expressed by β illustrated for circle, ellipse and circular sector in Table 1.

This reasoning based on 2, describing the quasi-3D flow model, fits well experimental observations of the ratio P_1/P_0 (Fig. 6) between mean pressures measured within (P_1) and upstream (P_0) from the constriction as a function of Reynolds number Re. Indeed, it is seen that the pressure drop within the constriction depends on both the cross-section shape and Reynolds number. The maximum pressure drop within the constriction is for all cases (121% for circle, 119% for ellipse and 114% for circular sector) smaller than 145%, the pressure drop associated with purely inertial flow. This confirms that viscosity affects the flow for all three constrictions at a rate determined by the cross-section shape (as expressed by β in 2). Moreover, note that the decreased magnitude of pressure drop reduction ordered by cross-section shape (ellipse then circular sector and then circle) is consistent with the increase of hydraulic diameter ($D_{el} < D_{cs} < D_{cl}$, see Table 3) for all Reynolds numbers Re.

The initial increase of the pressure drop with Reynolds numbers in the range $0 < Re < Re_t$, with Re_t denoting the Reynolds number associated with maximum pressure drop ($Re_t \approx 6000$ for circle, $Re_t \approx 7000$ for ellipse and $Re_t \approx 6700$ for circular sector), expresses the increasing impact of inertial flow effects compared to viscous flow effects expressed by Reynolds number increase [2]. On the other hand, for Reynolds numbers Re greater than Re_t the pressure drop is seen to reduce for all cases (cl, el and cs) indicating that an additional pressure recovery occurs likely due to the transition from laminar to turbulent flow which reduces the pressure drop with about 6% compared to its maximum value (116% for circle, 113% for ellipse and 108% for circular sector). The range of Reynolds numbers associated with the transitional flow regime depends on the cross-section shape as well since pressure recovery occurs *e.g.* more slowly for circle as for circular sector since 4% pressure recovery corresponds to $Re_t + 8000$ compared to $Re_t + 3000$, respectively (Fig. 6). The flow within the constriction remains laminar ($Re \ll Re_t$) for all assessed cross-section shapes as upstream pressure $P_0 < 150$Pa. The quasi-3D flow model is not expected to capture tendencies observed for Reynolds numbers associated with the transitional or turbulent flow regime since laminar flow is assumed in the quasi-3D model.

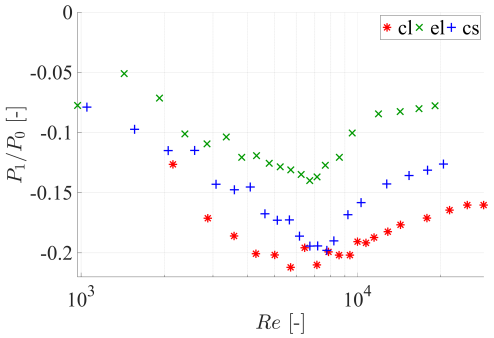

FIGURE 6 – Measured ratio P_1/P_0 as a function of Reynolds number Re for cross-section shapes : circle (cl - $*$), ellipse (el - $\times$) and circular sector (cs - +).

4.1.2 Velocity downstream from the constriction

For the assessed flow channel (Fig. 5), the jet is confined by the downstream tube of 15cm between $1 \times L_c$ up to $7 \times L_c$ which corresponds to at least 15 times the hydraulic diameter ($15 \times D_{cl}$ for circle, $22 \times D_{el}$ for ellipse and $21 \times D_{cs}$ for circular sector). In this case, the jet is likely to re-attach somewhere along the walls of the downstream tube due to mixing and expansion despite reduced flow entrainment due to confinement [2].

In order to illustrate jet development the longitudinal velocity profile $u(x)$ is measured along the centerline of the jet (Fig. 2) in the range $1 < x/L_c \leq 7$ (Fig. 5) while imposing upstream pressure $P_0 = 35$Pa resulting in laminar flow ($Re < Re_t$) within the constriction for all cases since $Re \approx 4200$ for circle, $Re \approx 2800$ for ellipse and $Re \approx 3000$ for circular sector. Measured longitudinal profiles normalised by the maximum velocity observed for the circular sector u^{cl}_{max} are shown in Fig. 7. Immediately downstream from the constriction exit the normalised velocity depends on the flow development within the constriction so that viscous effects – and hence the cross-section shape – contribute to shape the initial jet velocity which varies up to 8%. Note that the observed decrease of initial jet velocity ($u_{el} > u_{cs} > u_{cl}$ at $x/L_c \approx 1$) corresponds to the measured pressure drop increase ($(P_1/P_0)_{el} < (P_1/P_0)_{cs} < (P_1/P_0)_{cl}$ in Fig. 6). The initial velocity is maintained within the potential jet core of finite extent ($x_{pc} < 3 \times L_c$). The dynamics of the jet in both the potential core as well as in the decay region further downstream is observed to depend on the velocity field at the constriction exit and therefore on the cross-section shape. Indeed, the potential core extent

x_{pc} varies as a function of the cross-section shape of the constriction since its value increases with 59% from the ellipse to the circle ($x_{pc}/L_c = 2.6$ or $x_{pc}/D = 6.5$ for circle, $x_{pc}/L_c = 1.4$ or $x_{pc}/D = 5.2$ for ellipse and $x_{pc}/L_c = 1.6$ or $x_{pc}/D = 5.7$ for circular sector). The decay region of the ellipse exhibits velocity peaks in the range $2 \times L_c < x < 3 \times L_c$ (or $7.5 \times D < x < 11.2 \times D$) indicating axis switching of the jet whereas a continuous velocity decay is observed for the circle and circular sector although at a different rate since the decay is more rapid for circle than for circular sector. The observed velocity decay towards the flow channel's exit ($x/L_c = 7$) motivates the assumption of $P_d = 0$ at the channel's exit, which is confirmed by pressure measurements near the channel's exit, *i.e.* $P_2 = 0 \pm 3$Pa for $Re < Re_t$.

The quasi-3D model neglects jet dynamics since its outcome is assumed constant downstream from flow separation ($x = x_s$ in Fig. 2) corresponding to a stable non-expanding jet of non-viscous flow with an infinite potential core (x_{pc}^{∞} in Fig. 2). The model assumption of an infinite potential core x_{pc}^{∞} is not realistic since the measured potential core extent x_{pc} is finite $x_{pc} < 3 \times L_c$ for all cases. Therefore, the quasi-3D flow model is not expected to capture tendencies related to jet development since this is omitted in the model.

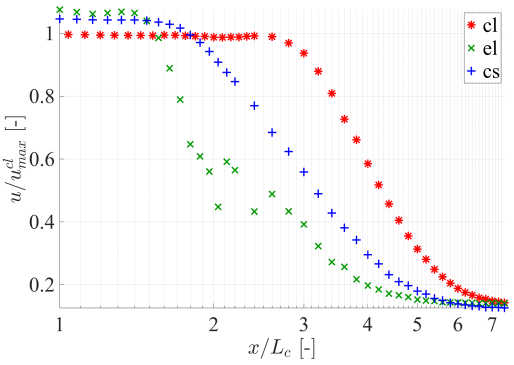

FIGURE 7 – Normalised measured longitudinal mean velocity u/u_{max}^{cl} for $P_0 = 35$Pa downstream from the constriction as a function of streamwise position x/L_c (Fig. 5) for cross-section shapes : circle (cl - $*$), ellipse (el - $\times$) and circular sector (cs - $+$).

4.2 Quantitative validation for $P_0 = 35$Pa

The quasi-3D laminar flow model takes into account the cross-section shape although it does not account for jet dynamics downstream from the constriction. The 3D flow simulations rely on a laminar flow description as well, but are expected to capture jet expansion mechanisms related to viscosity. Therefore, in order to evaluate the quasi-3D model, it is of interest to compare the model outcome with the simulated flow field as well as with experimental observations within the laminar flow regime ($Re < Re_t$). In the following, a comparison between modeled, simulated and measured flow features is presented for upstream pressure $P_0 = 35$Pa which is well within the range of upstream pressures ($P_0 < 150$Pa) for which $Re \ll Re_t$ for all cross-section shapes.

Modeled (subscript m) pressure distributions P_x, simulated (subscript s) pressure distributions P_x and experimentally (subscript e) observed pressures P_1 at the center of the constriction are plotted in Fig. 8 for all assessed cross-section shapes. Both modeled

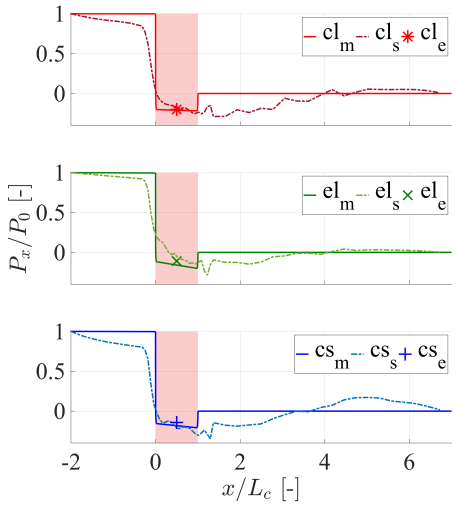

FIGURE 8 – Illustration of modeled (full line, subscript m) and simulated (dash-dotted line, subscript s) pressure distribution $P_x = P(x)$ normalized by the upstream pressure $P_0 = 35$Pa for cross-section shapes as a function of streamwise position x/L_c : circle (cl - top), ellipse (el - middle) and circular sector (cs - bottom). Measured pressures P_1 at $x/L_c = 0.5$ (symbol, subscript e) are also shown.

(overestimation $< 3\%$) and simulated (underestimation $< 5\%$) pressures result in an accurate estimation of the measured pressure drop (P_1/P_0) at the center of the constriction ($x/L_c = 0.5$) for all cross-section shapes. In addition, modeled and simulated pressure drops P_1/P_0 decreases when the cross-section is varied from ellipse to circular sector and to circle in agreement with experimental observations ($(P_1/P_0)_{el} < (P_1/P_0)_{cs} < (P_1/P_0)_{cl}$ in Fig. 6). Within the constriction ($0 \leq x/L_c \leq 1$) both the modeled and simulated pressure distribution decreases downstream from the constriction's inlet ($x = 0$). It is observed that the maximum difference between modeled and simulated pressure values within the constriction decreases from $< 25\%$ in the inlet region ($0 \leq x/Lc < 0.5$) to $< 10\%$ in the outlet region ($0.5 \leq x/Lc \leq 1$) indicating that the quasi-3D model provides only a rough approximation of flow phenomena near the constriction's inlet since it does not account for the presence of flow recirculation zones which occur due to the severity of the constriction (constriction degree reduces abruptly with more than 80% at $x = x_1$ in Fig. 2) [4]. Nevertheless, the overall agreement between modeled, simulated and measured pressures within the constriction shows that the quasi-3D model approach allows to maintain the model accuracy

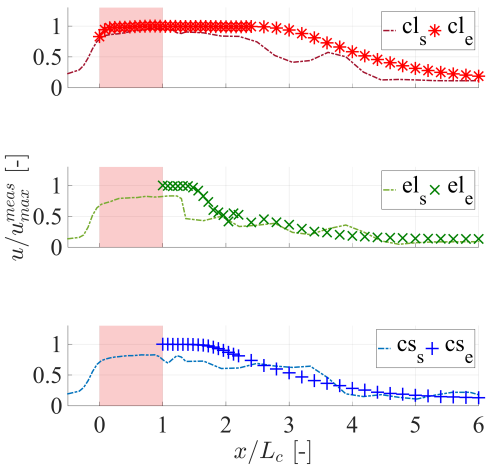

FIGURE 9 – Illustration of simulated (dash-dotted line, subscript s) and measured (symbol, subscript e) longitudinal velocity profile u along the centerline of the jet normalized by the maximum of the measured profile u_{max}^{meas} as a function of streamwise position x/L_c : circle (cl - top), ellipse (el - middle) and circular sector (cs - bottom).

regardless of the cross-section shape (even in the case of a severe constriction). Downstream from flow separation near the constriction's exit ($x \approx x_s$), the model outcome is constant and does not account for vortex formation, jet expansion and associated recirculation zones. These phenomena affect the simulated pressure distributions downstream from the constriction for all cross-section shapes since negative pressures are observed along the potential core of the simulated jet (up to $x/L_c \approx 3$, Fig. 9) whereas pressure recovery is observed as the flow expands further downstream (downstream from $x/L_c \approx 3$, Fig. 9). Nevertheless, from Fig. 9 is seen that both the initial jet velocity at the constriction's exit ($< 20\%$) as the potential core extent ($\approx 50\%$ when considering constant velocity) are underestimated when comparing simulated and measured values.

Modeled, simulated and measured spanwise velocity profiles are shown in Fig. 10. In general, it is seen that the simulated velocity profile underestimates the measured velocity ($< 20\%$) but since it accounts for the growth of the boundary layer it predicts an ideal core flow with constant velocity enveloped by a viscous boundary layer in agreement with experimental observations. The modeled velocity is estimated supposing a fully developed viscous velocity profile as a result no core region with constant velocity is observed and the velocity is overestimated at transverse positions within this core region. Nevertheless, it is seen that the quasi-3D model accounts for asymmetric boundary layer development as observed for the circular sector.

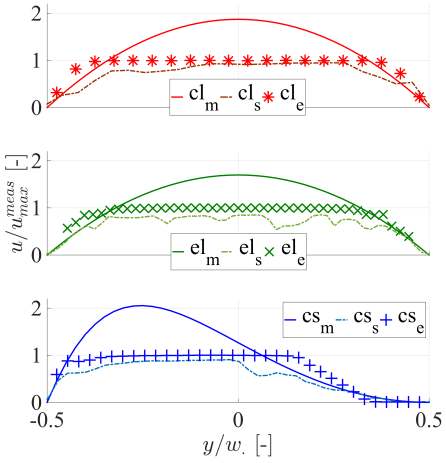

FIGURE 10 – llustration of modeled (full line, subscript m), simulated (dash-dotted line, subscript s) and measured (symbol, subscript e) spanwise velocity profiles u normalized by the maximum of the measured profile u_{max}^{meas} as a function of spanwise position $y/w_.$: circle (cl - top), ellipse (el - middle) and circular sector (cs - bottom).

5 Conclusion

The impact of the cross-section shape is shown experimentally for the pressure within the constriction and for the centerline velocity of the confined jet developing within the tube downstream from the constriction. Quasi-1D or 2D flow models commonly used in analytical models of fluid-structure interactions for physiological applications omit this potential influence of the cross-section shape. Therefore, a quasi-3D flow model is qualitatively and quantitatively validated against measured and simulated data. It is seen that the quasi-3D flow model captures main flow features within the constriction whereas downstream from the constriction the quasi-3D model approach does not hold since jet expansion is not accounted for.

Références

[1] C.S. Peskin. The immersed boundary method. *Acta numerica*, 11(0) :479–517, 2002.

[2] H. Schlichting and K. Gersten. *Boundary Layer Theory*. Springer, Berlin, 7th edition, 2000.

[3] A. Van Hirtum, B. Wu, X. Pelorson, and J. Lucero. Influence of glottal cross-section shape on phonation onset. *J. Acoust. Soc. Am.*, 136 :853–858, 2014.

[4] B. Wu. *The influence of the cross section shape on channel flow : modeling, simulation and experiment*. PhD thesis, Grenoble University, 2014.

[5] B. Wu, A. Van Hirtum, and X.Y. Luo. Pressure driven steady flow in constricted channels of different cross section shapes. *International Journal of Applied Mechanics*, 5(1) :1–19, 2013.